



**University of
Nottingham**

UK | CHINA | MALAYSIA

THE UNIVERSITY OF NOTTINGHAM

DEPARTMENT OF ELECTRICAL AND ELECTRONIC ENGINEERING

POWER SYSTEMS FOR AEROSPACE, MARINE & AUTOMOTIVE
APPLICATIONS

SPRING SEMESTER 2025

COURSEWORK 2

**Control System Design for an
Electromechanical Actuator**

AUTHOR THOMAS BULLOCK

STUDENT ID 20178937

Page Count: 20

Wednesday 30th April, 2025

Contents

1	Introduction	2
1.1	More-Electric Aircraft Concept	2
1.2	Role of Electromechanical Actuators	2
1.3	Aim & Objectives	2
2	EMA Technology Overview	3
2.1	EMA Principles and Architecture	3
2.2	Hydraulic and Electrohydrostatic Actuators	3
2.3	Motor & Power Electronics Selection	3
2.4	Mechanical & Control Aspects	4
3	EMA Control Design	4
3.1	Actuator Selection	4
3.2	Motor Selection	4
3.3	Modelling Constants	5
3.4	Plant Modelling	5
3.5	Control Design	7
3.5.1	Cascade Control	7
3.5.2	Control Design Requirements	7
3.6	Current Loop Design & Validation	8
3.6.1	Cross Link Compensation	8
3.6.2	Frequency-Domain Derivation the Current Loop	9
3.6.3	Anti-Windup	10
3.6.4	Current Results	10
3.7	Speed Loop Design & Validation	11
3.7.1	Speed Loop Transfer Function Derivation	11
3.7.2	Speed Results	12
3.8	Position Loop Design & Validation	14
3.8.1	Position Loop Transfer Function Derivation	14
3.8.2	Position Results	14
4	System Simulation & Results	15
4.1	Full Cascade Control System	16
4.2	Performance Validation	16
4.2.1	Current & Speed Validation	16
4.2.2	Position & Torque Validation	17
5	Advanced Topics	17
5.1	Time-Domain Derivation of the Current Loop	17
6	Conclusions	19
	References	19

1 Introduction

1.1 More-Electric Aircraft Concept

‘Traditional aircraft have relied heavily on mechanical, hydraulic and pneumatic systems to operate various functions including flight and environmental controls, wing ice protection and actuation systems. All of these critical flight operations derive their power from the engine, shown in Figure 1a. While effective, these systems are heavy, inefficient and prone to maintenance challenges [1]. The emergence of the more electric aircraft (MEA) concept, shown in Figure 1b, addresses these limitations by replacing the hydraulic, pneumatic and mechanical functions with electrical counterparts. The benefits of a more electric aircraft are increased performance, decreased maintenance costs and emissions [2]. The main performance enhancement is achieved by eliminating the pneumatic system, thereby removing the requirement for bleed air. This ensures that the mass flow rate of air through the engine remains unchanged, resulting in a significant increase in thrust at a given throttle setting. The elimination of hydraulic and mechanical systems leads to an overall weight reduction, thereby enhancing the aircraft’s efficiency.’ - reproduced from my essay in coursework 1.

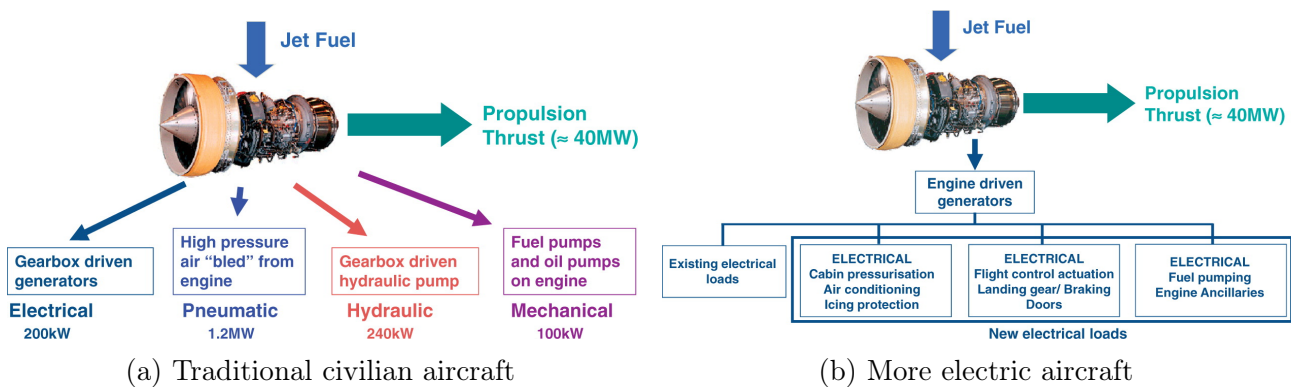


Figure 1: Power sources on traditional civilian and a MEA. Reproduced from [3].

1.2 Role of Electromechanical Actuators

‘The transition from conventional aircraft to MEA systems involves key technological advancements. Hydraulic power, traditionally utilised for controlling critical flight surfaces, is replaced by electromechanical actuators (EMAs), shown in Figure 2a. EMAs convert electrical energy into mechanical motion, typically using an electric motor coupled with a mechanical transmission, such as a ball screw, to drive control surfaces.’ - reproduced from my essay in coursework 1.

1.3 Aim & Objectives

The aim of this coursework is to develop and demonstrate a comprehensive understanding of EMA systems and their control, specifically within the context of MEA applications.

The objectives are to:

- Develop a good understanding of EMA principles and architectures.
- Investigate EMA technologies.
- Select an appropriate actuator based on a given specification and justify the choice with technical reasoning.
- Design a multi-stage cascade control system, that satisfies the specified performance criteria.

- Implement and simulate the complete control system using MATLAB[®]/SIMULINK[®].
- Evaluate the control system's performance against the required actuator specifications.

2 EMA Technology Overview

2.1 EMA Principles and Architecture

EMAs are electrically powered devices that convert electrical energy into mechanical motion using an electric motor and a mechanical transmission. Unlike conventional hydraulic actuators, EMAs do not use any hydraulic fluid, eliminating the complex piping, central pumps, and leak risks of fluid power. Instead, an electric motor drives the control surface through a gear and screw mechanism, providing the force and displacement needed for aileron deflection [4].

2.2 Hydraulic and Electrohydrostatic Actuators

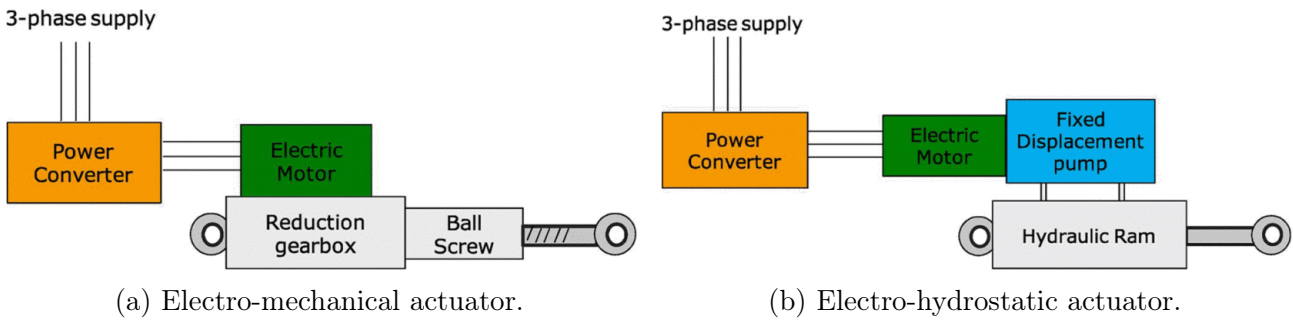


Figure 2: Reproduced from [5].

Traditional aircraft have historically used hydraulic servo actuators powered by centralised hydraulic systems to move flight control surfaces. While effective, this approach has both advantages and disadvantages compared to electromechanical actuators (EMA) and electrohydrostatic actuators (EHA). EHAs, shown in Figure 2b, are self-contained units that integrate an electric motor, hydraulic pump, and actuator.

Eliminating hydraulic fluid and extensive piping offers significant benefits, including enhanced safety, increased reliability, and reductions in weight and maintenance requirements. Without hydraulic fluid, the risk of leaks and fire hazards is minimised, and overall maintenance costs are lower. EMAs also draw electrical power only when required, improving energy efficiency relative to continuously pressurised hydraulic systems [2].

However, EMAs currently face limitations in applications demanding extremely high forces, such as landing gear actuation. Their mechanical drivetrain can introduce backlash, which is mechanical play in gears or screw threads, and presents a risk of jamming if components seize. Additionally, thermal management becomes a critical issue; without fluid to carry heat away, careful design is needed to ensure sufficient cooling for the motor and drive electronics [4].

2.3 Motor & Power Electronics Selection

EMAs typically employ three-phase brushless permanent magnet machines, selected for their high torque-to-weight ratio and reliability. Permanent magnet machines (PMM) utilise permanent magnets embedded within the rotor, eliminating the need for rotor windings and thereby reducing power losses. The absence of brushes and commutators significantly lowers maintenance requirements while enhancing reliability and service life which are critical attributes for aviation applications.

EMAs incorporate dedicated power electronic drives as part of the electronic control unit (ECU). These converters regulate voltage and frequency through high-frequency switching to control motor speed and torque. In modern designs, the power electronics and control systems are integrated directly with the actuator, resulting in a highly compact and efficient unit [6].

2.4 Mechanical & Control Aspects

Electromechanical actuators for aileron control are typically designed to produce linear output motion. The rotary motion generated by the electric motor is converted into linear displacement through a gearbox and screw mechanism. As the motor rotates, either the screw or the nut translates linearly, functioning similarly to a jack to push or pull the aileron's control linkage. The actuator's output rod connects to the aileron via a hinge or bell crank, thereby rotating the control surface. To ensure the aileron maintains its position when the EMA is unpowered, a brake or locking mechanism is often incorporated.

EMAs utilise closed-loop control systems based on a cascade control structure, which will be implemented later in this report [4].

A notable industrial example of EMA application is found on the Boeing 787, where EMAs are used to drive spoiler panels for roll control. Similarly, the Airbus A380 and A350 employ EMAs to control the wing leading-edge slats [4].

3 EMA Control Design

You might have to zoom in on some of the figures. Most of them have scaled graphics so it should be okay.

3.1 Actuator Selection

Table 1: Actuator Requirements

Application	Stroke [mm]	Velocity [mm s ⁻¹]	Rated Force [N]
Aileron	140	220	5000

Table 2: GS40-0602 Performance Specification

Model	Stroke [mm]	Velocity [mm s ⁻¹]	Rated Force [N]
GS40-0602	152	254	5703

The GS40-0602 was selected as the actuator, as it meets all the requirements outlined in Table 1.

3.2 Motor Selection

Based on the selected actuator, a corresponding motor was selected.

To confirm whether the motor was capable of meeting the requirements, a series of calculations were performed.

For the load of 5000 N, the motor has to provide an equivalent torque of:

$$T_L = \frac{F \cdot L}{2\pi \cdot \eta} = \frac{5000 \cdot 5.08 \times 10^{-3}}{2\pi \cdot 1} = 4.04 \text{ N m} \quad (1)$$

The linear velocity of a roller screw is related to the mechanical speed and the lead by:

$$\omega_m = \frac{\nu \cdot 2\pi}{L} = 272 \text{ rad s}^{-1} \quad (2)$$

Table 3: GS40 H8 RMS Sinusoidal Commutation Motor Parameters

Parameter	Value
Continuous motor torque [N m]	5.85
Torque constant (k_t) [N m/A]	1.82
Speed at bus voltage [rad s ⁻¹]	314
Continuous current rating [A]	6.43
Peak current rating [A]	6.43
Electrical time constant [ms]	2.02
Damping constant [N m/krpm]	0.37
Bus voltage Vdc [V]	460
Voltage constant [V rms/krpm]	114.70
Voltage constant (peak) [V/krpm]	162.22
Pole configuration [-]	8
Resistance (L-L) [Ω]	4.81
Inductance (L-L) [mH]	9.72
Armature Inertia (J) [kg m ²]	0.001718
Screw Lead (L_{screw}) [mm]	5.08

The selected machine provides continuous motor torque of 5.85 N m and angular velocity of 314 rad s⁻¹ which satisfies the results from Equations 1 and 2.

3.3 Modelling Constants

A range of modelling constants required for the control design are presented below:

$$\psi_m = \frac{2 \cdot k_t}{3 \cdot p} = 0.303 \text{ Wb} \quad (3)$$

$$R_s = \frac{R_{LL}}{2} = 2.405 \Omega \quad (4)$$

$$L_s = \frac{L_{LL}}{2} = 4.9 \times 10^{-3} \text{ H} \quad (5)$$

$$\omega_{\max} = \frac{3000 \cdot 2\pi}{60} = 314 \text{ rad s}^{-1} \quad (6)$$

$$i = \frac{2\pi}{\text{screw lead}} = 1.24 \times 10^3 \text{ rad m}^{-1} \quad (7)$$

3.4 Plant Modelling

To design the control architecture, the EMA must first be represented as a plant. The actuator is driven by a permanent magnet machine (PMM), which is modelled in the rotating frame reference using the $d - q$ -axis. For the purpose of this report, it is assumed that $L_d = L_q = L_s$. Therefore, the plant equations become:

Electrical Model

$$\begin{aligned} v_d &= R_s i_d + L_s \frac{di_d}{dt} - \omega_e L_s i_q \\ v_q &= R_s i_q + L_s \frac{di_q}{dt} + \omega_e L_s i_d + \omega_e \psi_m \end{aligned} \quad (8)$$

Where:

- v_d, v_q : voltages in the $d - q$ reference frame [V]
- i_d, i_q : $d - q$ axis stator currents [A]
- R_s : stator resistance [Ω]
- L_s : stator inductance [H]
- ω_e : electrical angular speed of the rotor [rad s^{-1}]
- ψ_m : permanent magnet flux linkage [Wb]

Mechanical Model

The motor torque is produced mainly by the q -axis current, and is given by:

$$T_m = \frac{3}{2} p \psi_m i_q \quad (9)$$

Where:

- T_m : electromagnetic torque [N m]
- p : number of pole pairs [-]

The relationship in Equation 9 highlights that the q -axis current directly controls torque, making it the primary focus of the speed control loop.

The motor's mechanical behaviour follows Newton's law:

$$J \frac{d\omega_m}{dt} = T_m - T_L \quad (10)$$

Where:

- ω_m : mechanical angular velocity [rad s^{-1}]
- T_L : load torque
- J : moment of inertia [kg m^2]

Finally, to link motor speed with position:

$$i \frac{d\delta}{dt} = \omega_m \quad (11)$$

Where:

- i : mechanical transmission ratio

This full set of equations forms the basis of the plant used in SIMULINK[®] which can be seen in Figure 3.

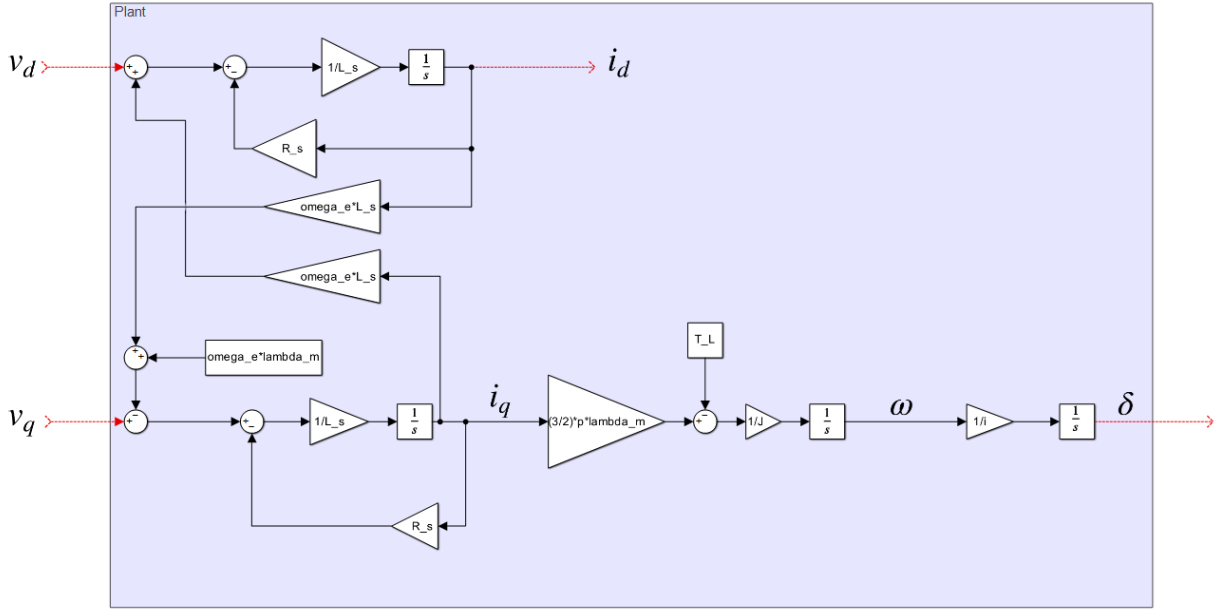


Figure 3: SIMULINK[®] diagram of the PMM as plant of EMA control. Constructed in the time domain.

3.5 Control Design

3.5.1 Cascade Control

A cascade control strategy was implemented for the electromechanical actuator, comprising nested current, speed, and position feedback loops. Each loop was designed with progressively lower bandwidth, ensuring that inner loops respond significantly faster than their outer counterparts. This configuration allows each loop to correct its own errors before they propagate, with the output of each loop serving as the reference input for the next inner loop [7]. Proportional-integral (PI) controllers were used at each level due to their ability to provide fast response while eliminating steady-state error, which is proven in section 5.1.

The outermost loop regulates position by comparing the desired and actual positions and generating a speed reference via a PI controller. The speed loop, nested within the position loop, compares this reference with the measured velocity and generates a new current reference (representing the torque demand – see Equation 9), which is passed to the current controller. Finally, the innermost current loop tracks this reference by comparing the reference current with the actual motor current and regulating the voltage input to the motor driver. The resulting current directly influences torque production, which in turn alters speed and position.

This hierarchical control structure offers significant benefits. By tuning each loop to its respective dynamic timescale, with the current loop operating at the highest bandwidth, the system ensures rapid disturbance rejection and enhanced stability. The cascade design also enables accurate tracking of position commands and robust control under varying load conditions, which is critical in aerospace applications [7].

3.5.2 Control Design Requirements

The minimum required bandwidth of the position loop was estimated using the time requirement for the maximum displacement of the EMA such that:

$$t_{\max} = \frac{\text{stroke}}{\text{max speed}} = \frac{0.14 \text{ m}}{0.22 \text{ m/s}} \approx 0.636 \text{ s} \Rightarrow f_{\min} = \frac{1}{10 \cdot t_{\max}} \approx 0.157 \text{ Hz} \quad (12)$$

However, based on tuning guidelines, a position loop bandwidth of $f_{\text{pos}} = 3 \text{ Hz}$ was selected to balance responsiveness and stability.

To ensure timescale separation and loop stability, each inner loop was designed to be approximately ten times faster than its outer counterpart. Therefore, the speed loop bandwidth was selected as:

$$f_{\text{speed}} = 10 \cdot f_{\text{pos}} = 30 \text{ Hz} \quad \text{and} \quad f_{\text{current}} = 10 \cdot f_{\text{speed}} = 300 \text{ Hz}$$

These values enable rapid current response, precise speed tracking, and smooth position response. The current and speed controllers were initially designed with a damping factor of $\zeta = 0.707$, which corresponds to quick response with a minimal overshoot in second-order system behaviour. The damping ratio for the position loop was selected to be $\zeta = 1$ which corresponds to critically damped, ensuring the quickest settling time without overshoot. In this context, overshoot is something to be critically aware of in the position loop.

This bandwidth and damping framework forms the basis for the controller parameter calculations and simulations presented in the following sections.

Table 4: Control Design Requirements Summary

Control Loop	Bandwidth [Hz]	Damping Factor [ζ]
Position	3	1
Speed	30	0.707
Current	300	0.707

3.6 Current Loop Design & Validation

3.6.1 Cross Link Compensation

In a permanent magnet machine, the $d - q$ axis equations are coupled due to rotational effects, meaning a change in one axis affects the other. This complicates controller design, as the system becomes as a MIMO (Multi-Input, Multi-Output) system. To simplify this, cross-coupling compensation is applied by feeding forward the coupling terms and subtracting them from the controller input. This effectively decouples the axes, allowing each to be treated as independent systems. The compensation works by cancelling the dynamic cross terms, thereby reshaping the plant into two single-input, single-output systems that are much easier to control using standard PI controllers.

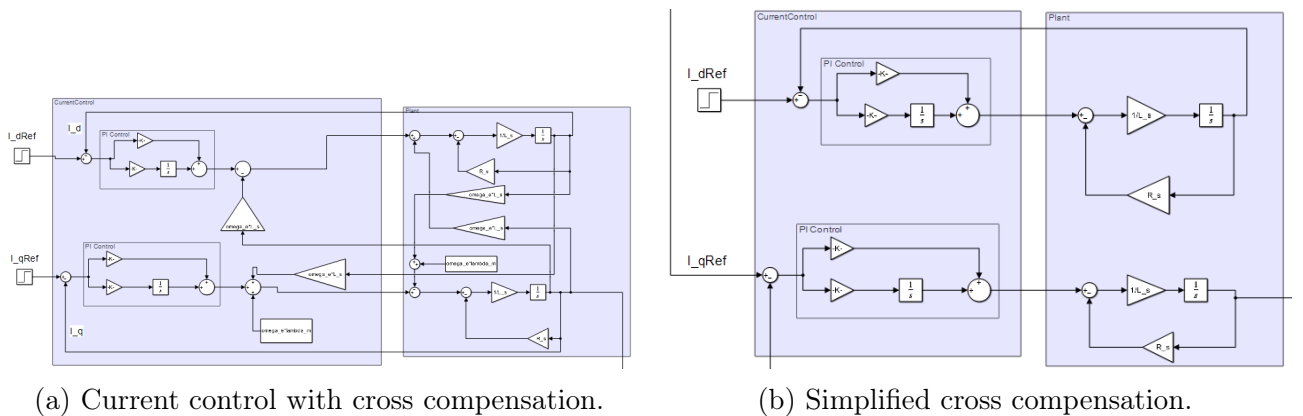


Figure 4: The current control with cross compensation. These two block diagrams are equivalent.

3.6.2 Frequency-Domain Derivation the Current Loop

The PI controller is given by:

$$W_{cc}(s) = K_{Pcc} + \frac{K_{Icc}}{s} \quad (13)$$

The plant model of the motor phase is:

$$W_{\text{plant}}(s) = \frac{1}{L_s s + R} \quad (14)$$

The closed-loop transfer function is defined as:

$$W_{CL}(s) = \frac{W_{cc}(s) \cdot W_{\text{plant}}(s)}{1 + W_{cc}(s) \cdot W_{\text{plant}}(s)} \quad (15)$$

Substitute both terms:

$$W_{cc}(s) \cdot W_{\text{plant}}(s) = \left(K_{Pcc} + \frac{K_{Icc}}{s} \right) \cdot \frac{1}{L_s s + R} \quad (16)$$

Multiply through:

$$= \frac{K_{Pcc}s + K_{Icc}}{s(L_s s + R)} = \frac{K_{Pcc}s + K_{Icc}}{L_s s^2 + Rs} \quad (17)$$

Now substitute this into the closed-loop formula:

$$W_{CL}(s) = \frac{\frac{K_{Pcc}s + K_{Icc}}{L_s s^2 + Rs}}{1 + \frac{K_{Pcc}s + K_{Icc}}{L_s s^2 + Rs}} \quad (18)$$

Bring to a common denominator:

$$W_{CL}(s) = \frac{K_{Pcc}s + K_{Icc}}{L_s s^2 + Rs + K_{Pcc}s + K_{Icc}} \quad (19)$$

Group and simplify the denominator:

$$W_{CL}(s) = \frac{K_{Pcc}s + K_{Icc}}{L_s s^2 + (R + K_{Pcc})s + K_{Icc}} \quad (20)$$

Finally, divide numerator and denominator by L_s to match second-order form:

$$W_{CL}(s) = \frac{\frac{K_{Pcc}}{L_s}s + \frac{K_{Icc}}{L_s}}{s^2 + \frac{K_{Pcc} + R}{L_s}s + \frac{K_{Icc}}{L_s}} \quad (21)$$

Compare with the standard second-order system form:

$$i''(t) + 2\xi\omega_0 i'(t) + \omega_0^2 i(t) = c \quad (22)$$

Matching coefficients:

$$\frac{R_s + K_{pcc}}{L} = 2\xi\omega_0 \quad (23)$$

$$\frac{K_{icc}}{L} = \omega_0^2 \quad (24)$$

Therefore, the PI gains for the current control are:

$$K_{icc} = L\omega_0^2 = 1.73 \times 10^4 \quad (25)$$

$$K_{pcc} = 2\xi\omega_0 L - R_s = 10.5 \quad (26)$$

The result in Figure 6a, shows that the control system performs well and tracks its rated current virtually instantly. Interestingly the overshoot is not as expected. Rather than 5%, the overshoot is closer to 12%. To determine why this is occurring the transfer function for the current loop must be investigated.

Equation 21, highlights a zero which occurs at $s = -\frac{K_{icc}}{K_{pcc}}$. While zeros don't effect the stability of a system, they do introduce additional dynamics that affect the transient response. While the system poles determine the natural response, the zero distorts the transient by introducing a derivative-like effect, causing a steeper initial rise and increased overshoot [7]. This effect is clearly seen when comparing the response of the real PI-controlled system to an ideal second-order system with identical poles but no zero, as shown in Figure 6a.

3.6.3 Anti-Windup

Anti-windup is a control strategy used to prevent the integrator in a PI controller from accumulating excessive error when the actuator output is saturated and can no longer follow the control signal. Without anti-windup, the integrator continues to build up error, even though the actuator is at its physical limit, leading to delayed recovery and overshoot once the error reverses. The model in Figure 5 implements clamping anti-windup by comparing the unsaturated and saturated controller outputs to detect when saturation occurs. It simultaneously checks if the error has the same sign as the controller output, indicating that the integrator is pushing the output further in that same direction. If both conditions are true, a logical AND gate triggers a switch that zeroes the integrator input, effectively halting the integration component of the PI controller. This ensures that the integrator doesn't 'wind up', and that it can immediately begin to decrease when the error changes sign or the controller leaves saturation.

3.6.4 Current Results

The controller demonstrates strong performance. As shown in Figure 6a, the system tracks the reference current with minimal, though slightly higher than expected overshoot. This behavior was previously discussed and is attributed to the presence of a zero in the transfer function. The effect of this zero is evident when compared to the ideal second-order system with identical poles. The anti-windup mechanism also performs effectively, as illustrated in Figure 6b, where the clamped controller responds to a step change significantly faster after saturation than the non-clamped version. While the initial reference current of 500 A is unrealistic, it was intentionally chosen to clearly demonstrate the anti-windup functionality.

Figure 6a demonstrates that the current controller achieves the intended bandwidth. Using the standard approximation:

$$f_0 \approx \frac{0.35}{t_r} = \frac{0.35}{0.0012} \approx 300 \text{ Hz} \quad (27)$$

Where t_r is the rise time, the calculated bandwidth closely aligns with the design target of 300 Hz. While the presence of a zero in the transfer function introduces some deviation in the transient response, its impact on overall bandwidth is limited.

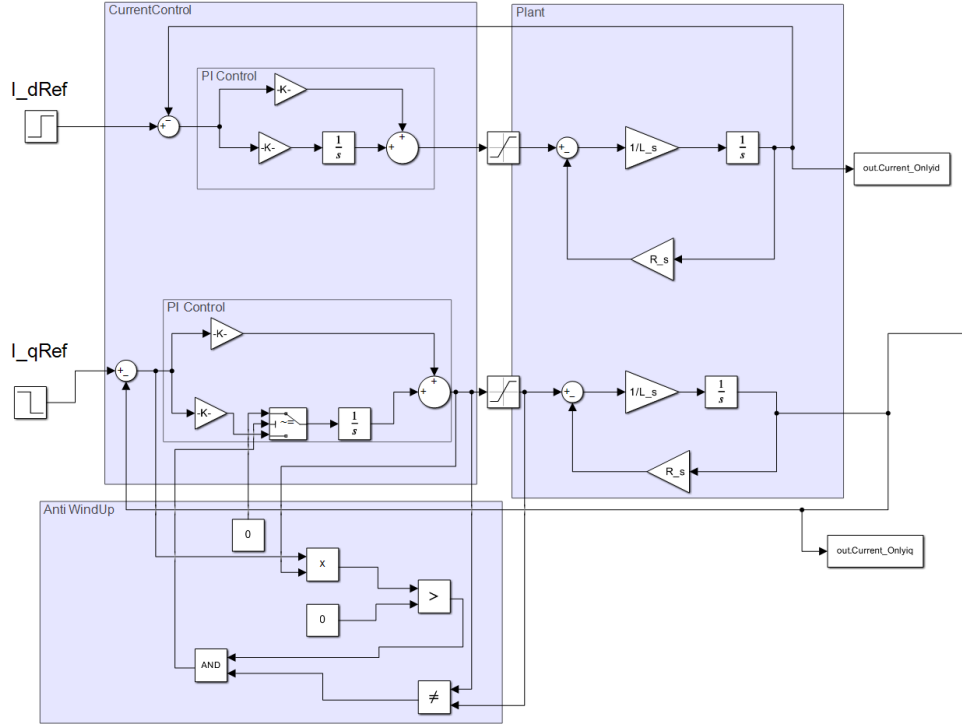


Figure 5: SIMULINK[®] model of the current loop. The voltage was clamped at ± 265.2 V.

3.7 Speed Loop Design & Validation

3.7.1 Speed Loop Transfer Function Derivation

Starting from the mechanical dynamics of the system:

$$J \frac{d\omega(t)}{dt} = T - T_L \quad (28)$$

In the Laplace domain:

$$\omega(s) = \frac{T(s) - T_L(s)}{J_s} \quad (29)$$

Assuming the torque is produced purely by the i_q current component:

$$\omega(s) = \frac{\frac{3}{2} p \lambda_m i_q(s)}{J_s} \quad (30)$$

Thus, the plant transfer function becomes:

$$W_{\text{plant}}(s) = \frac{\omega(s)}{i_q(s)} = \frac{\frac{3}{2} p \lambda_m}{J_s} \quad (31)$$

The PI controller is:

$$W_{cc}(s) = K_{p\omega} + \frac{K_{i\omega}}{s} \quad (32)$$

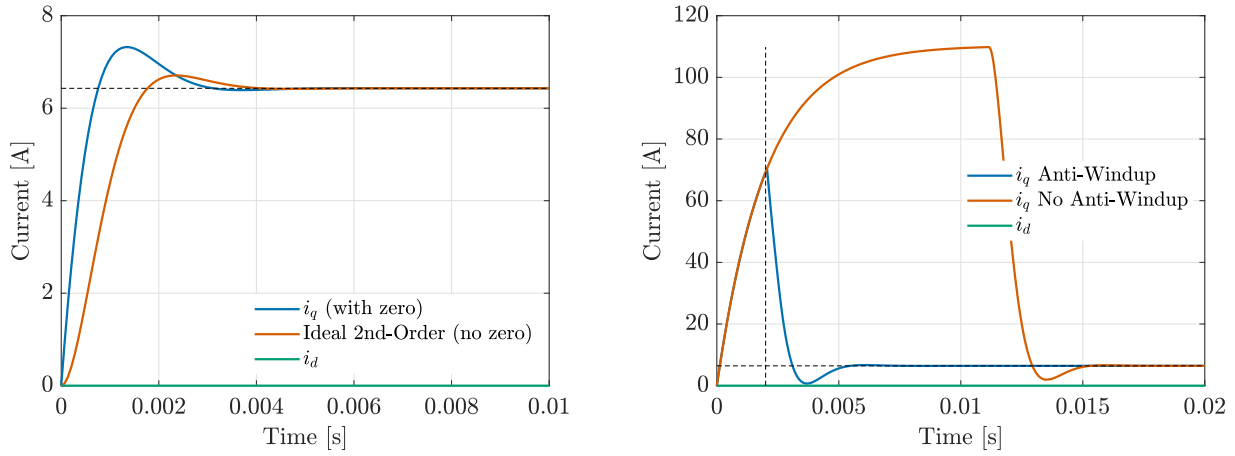
Therefore, the closed-loop transfer function becomes:

$$W_{CL}(s) = \frac{(K_{P\omega}s + K_{I\omega}) \cdot \frac{K_t}{J}}{s^2 + \frac{K_{P\omega}K_t}{J}s + \frac{K_{i\omega}K_t}{J}} \quad (33)$$

The gains can be selected as:

$$K_{P\omega} = 2\omega_0\zeta \cdot \frac{J}{K_t} = 0.25 \quad (34)$$

$$K_{I\omega} = \omega_0^2 \cdot \frac{J}{K_t} = 34 \quad (35)$$



(a) The step response of the current to the rated value, compared to an ideal 2nd order system with the same poles, highlighting the affects of the zero on the transient response.

(b) Comparison of current response with and without anti-windup. The system is subjected to an initial large current reference of 500 A, followed by a step down to the rated current of 6.43 A at 0.002 seconds.

Figure 6

3.7.2 Speed Results

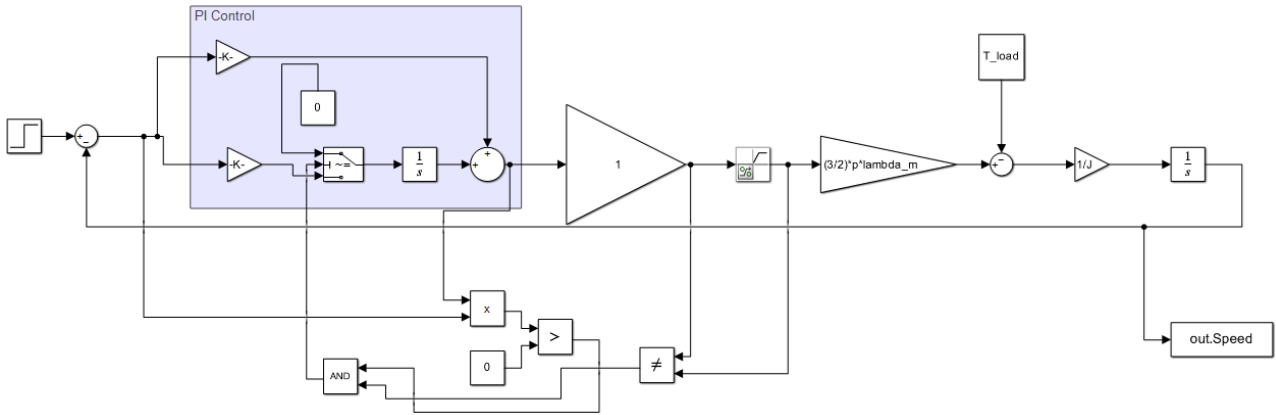


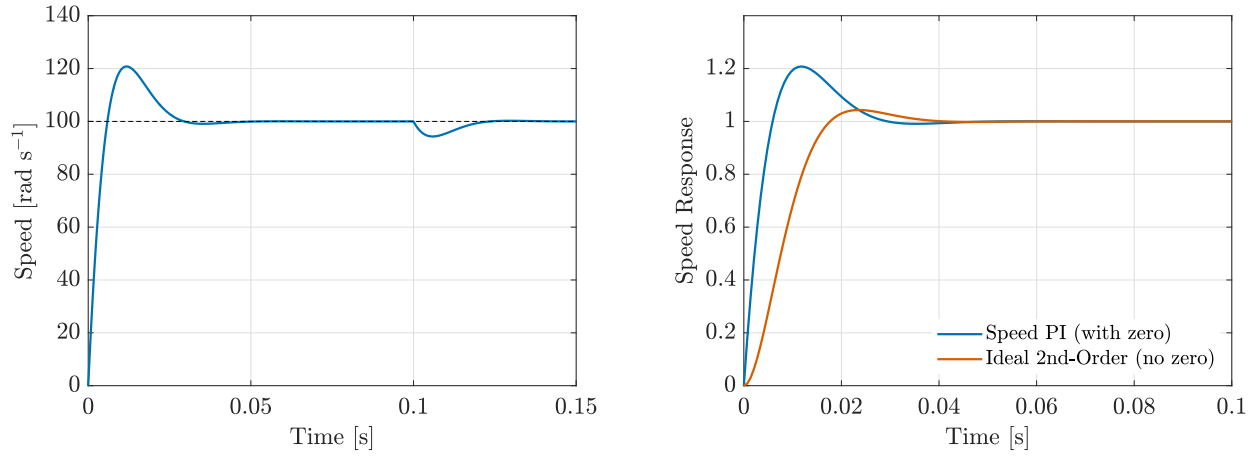
Figure 7: SIMULINK[®] model of the speed control loop. The current loop is represented by a unity gain.

The speed control performs well. Figure 8a shows the system responding to a step load torque at 0.1 seconds, demonstrating its ability to reject a constant disturbance. As with the current loop, the transfer function includes a zero, and its impact on the transient response is clearly illustrated in Figure 8b.

Figure 8a confirms that the speed loop bandwidth closely matches the design target. While the presence of a zero in the transfer function slightly distorts the transient response, its effect on bandwidth is minimal in this case. The closed-loop bandwidth can be approximated using the empirical relation:

$$f_0 \approx \frac{0.35}{t_r} = \frac{0.35}{0.012} \approx 30 \text{ Hz} \quad (36)$$

This result aligns well with the desired speed loop bandwidth of 30 Hz, validating the controller tuning.



(a) The step response of the speed to 100 rad s^{-1} with step load torque at 0.1 s.

(b) The step response of the speed, compared to an ideal 2nd order system with the same poles, highlighting the effects of the zero on the transient response.

Figure 8

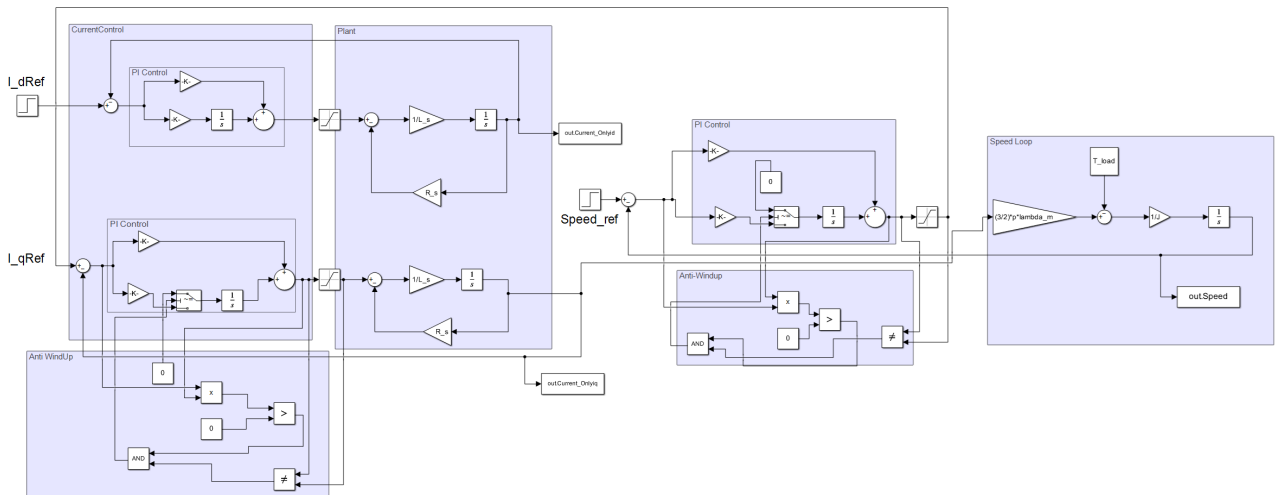
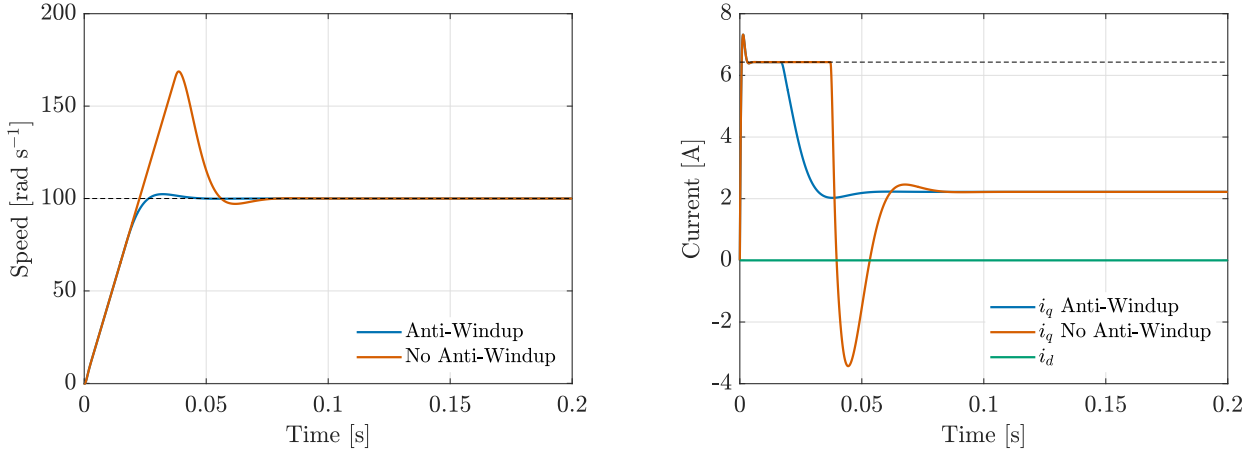


Figure 9: SIMULINK[®] model of the combined speed and current control loops. The speed controller generates a current reference, which is clamped to the rated current limits of $\pm 6.43 \text{ A}$.

Figure 10a illustrates the effect of the anti-windup mechanism when the speed is subjected to a step reference of 100 rad s^{-1} . The system performs well: the rise time remains unchanged, and the overshoot is minimal compared to the response without anti-windup. Figure 10b shows the corresponding current response. Without anti-windup, the system reacts more slowly, as it must first overcome the accumulated integration error. With anti-windup in place, the system responds more quickly and effectively, as the integrator is prevented from building excessive error during saturation, allowing for a smoother recovery once the actuator is back within range.



(a) The step response of the speed to 100 rad s^{-1} with and without anti-windup. (b) The behaviour of the i_q current for Figure 10a.

Figure 10

3.8 Position Loop Design & Validation

3.8.1 Position Loop Transfer Function Derivation

The closed loop transfer function and PI controller transfer function are the same as in Sections 3.6.2 and 3.7.1.

$$\frac{\varphi(s)}{\varphi^*(s)} = \frac{(K_{pp}s + K_{Ip})}{s^2 + \frac{K_{pp}}{i}s + \frac{K_{Ip}}{i}} \quad (37)$$

$$s^2 + 2\zeta\omega_0 s + \omega_0^2 = 0 \quad (38)$$

$$K_{pp} = 2\zeta\omega_0 i = 4.66 \times 10^4 \quad (39)$$

$$K_{Ip} = \omega_0^2 i = 4.39 \times 10^5 \quad (40)$$

A first-order lag block was applied after the step position reference. This ensured that the position error did not instantly reach its maximum value, thereby minimising the transient excitation of the zero in the closed loop transfer function, as illustrated in Figure 12a. The lag block introduces a dynamically rising reference signal that smoothly decays toward the final step value. This approach provides a more gradual introduction of error into the system and effectively suppresses the overshoot typically caused by the closed loop zero. In this application, it is critical that the EMA does not overshoot the target position. Through iterative tuning, the optimal lag block transfer function was determined to be:

$$\frac{1}{\frac{2.62}{\omega_{pos}}s + 1} \quad (41)$$

3.8.2 Position Results

$$f_0 \approx \frac{0.35}{t_r} = \frac{0.35}{0.11} \approx 3 \text{ Hz} \quad (42)$$

The results confirmed the theoretical expectations. Figure 12b shows that the position tracks the reference input effectively, with no overshoot. As seen in Figure 12a, the response appears to be slightly overdamped. It is clear from Equation 42 that the controller performs with the designed bandwidth.

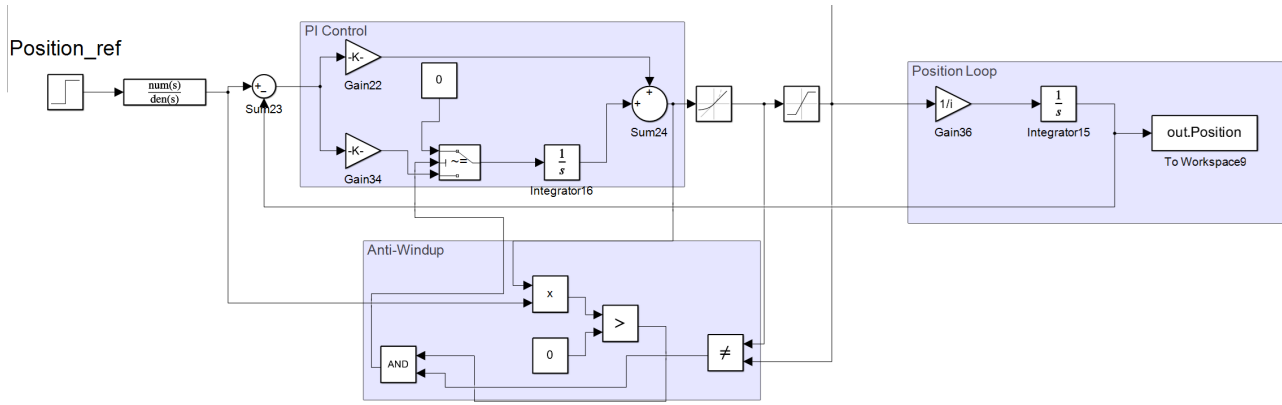
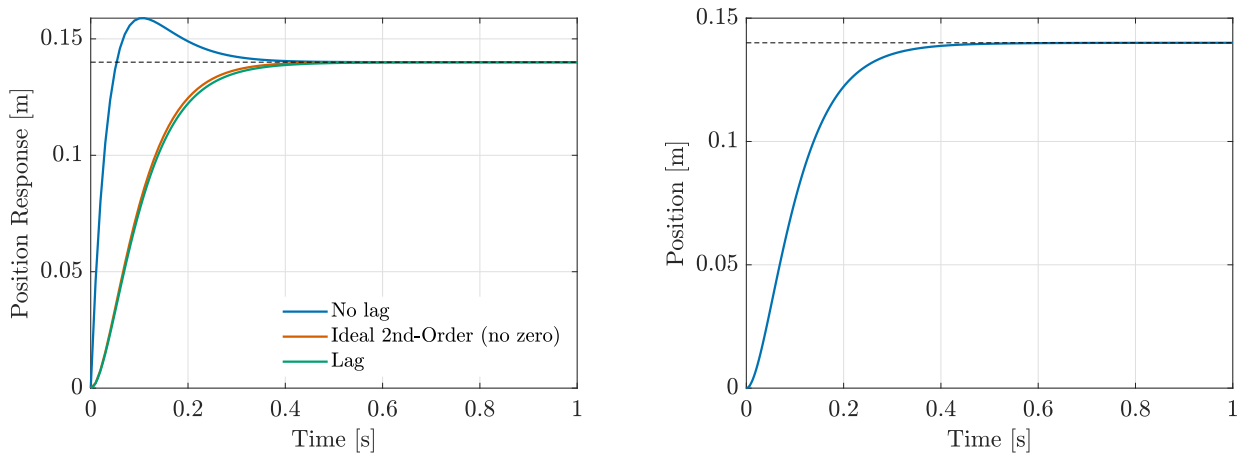


Figure 11: SIMULINK[®] of the position loop. The PI controller outputs a speed reference, which is clamped to the maximum speed of $\pm 272 \text{ rad s}^{-1}$. Additionally, the rate of change of the speed reference is limited based on the motor's maximum allowable acceleration.



(a) Position step response comparison. The figure compares the position response with and without a first-order lag block applied to the reference input, alongside an ideal second-order system for reference.

(b) Final position response. Step position reference equal to the EMA rated stroke of 140 mm.

Figure 12: Position Step Response. The response of the position loop to a step input, without the influence of additional effects such as actuator saturation.

4 System Simulation & Results

Table 5: Summary of Saturation Limits Implemented in the Control Model

Saturation	Limit applied	Justification
Voltage	$\pm 265.2 \text{ V}$	Inverter cannot output more than $\frac{V_{dc}}{\sqrt{3}}$ per phase.
Current	$\pm 5.25 \text{ A}$	Allows for the overshoot to be under the rated current of 6.43 A.
Mechanical speed	$\pm 272 \text{ rad s}^{-1}$	Derived in Equation 2.

applied at 0.8 seconds, the current increases sharply to supply the necessary force to counteract the external load torque with an equal and opposite reaction.

Figure 14b shows that the speed response remains within the operating limit of $\pm 272 \text{ rad s}^{-1}$. The actuator accelerates sharply at the start, rapidly reaching its maximum speed and entering saturation. Once the position reference is reached, the speed promptly decelerates to zero, aided by the anti-windup mechanism. The impact of the applied load torque is visible in the response, but its effects are swiftly rejected by the system.

4.2.2 Position & Torque Validation

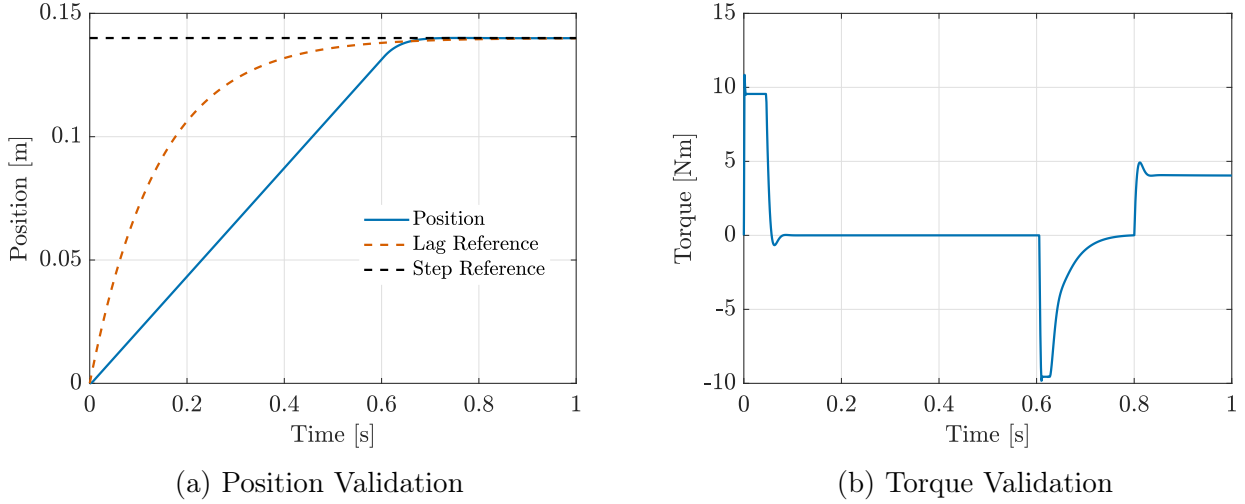


Figure 15

Figure 15a presents the position response alongside the reference signal supplied to the PI controller, comparing cases with and without the lag block. The actuator accurately tracks its maximum rated stroke with **no overshoot**, settling at approximately 0.71 s. Theoretically, the settling time should be 0.636 s, as derived from Equation 12, however this value represents the limiting case. The slight increase in settling time is attributed to the system's limited bandwidth and the presence of the lag block, which was introduced specifically to eliminate overshoot in the position response. If the system had infinite bandwidth, the settling time would match the theoretical value of 0.636 s.

Figure 15b illustrates the torque response, which mirrors the shape of the current response, scaled by the torque constant, as expected. The torque remains well within the operating range of $\pm 11.7 \text{ N m}$. The response behaves as intended, clearly demonstrating that the controller effectively and rapidly compensates for the applied load torque of -4.04 N m by applying an equal and opposite force, successfully cancelling out the disturbance.

5 Advanced Topics

5.1 Time-Domain Derivation of the Current Loop

A time-domain analysis of the current control loop is included. This not only is confirmed by the frequency derivation in Section 3.6.2, also mathematically demonstrates the key advantage of the PI controller which is present in all the control loops: **zero steady-state error**.

The decoupled current loop (after cross-coupling compensation) is modelled as a first-order equation:

$$v(t) = R_s i(t) + L \dot{i}(t) \quad (43)$$

Using a PI controller:

$$v(t) = K_p e(t) + K_i \int_0^t e(\tau) d\tau \quad (44)$$

where the error is defined as:

$$e(t) = i_{\text{ref}}(t) - i(t) \quad (45)$$

Substitute the PI controller into the plant:

$$L i'(t) = -R_s i(t) + K_p (i_{\text{ref}}(t) - i(t)) + K_i \int_0^t (i_{\text{ref}}(\tau) - i(\tau)) d\tau \quad (46)$$

Differentiate both sides with respect to time:

$$L i''(t) = -R_s i'(t) + K_p (i_{\text{ref}}'(t) - i'(t)) + K_i (i_{\text{ref}}(t) - i(t)) \quad (47)$$

Rearrange:

$$i''(t) + \frac{R_s + K_p}{L} i'(t) + \frac{K_i}{L} i(t) = \frac{K_p}{L} i_{\text{ref}}'(t) + \frac{K_i}{L} i_{\text{ref}}(t) \quad (48)$$

Compare with the standard second-order system form:

$$i''(t) + 2\xi\omega_0 i'(t) + \omega_0^2 i(t) = c \quad (49)$$

Matching coefficients:

$$\frac{R_s + K_p}{L} = 2\xi\omega_0 \quad (50)$$

$$\frac{K_i}{L} = \omega_0^2 \quad (51)$$

Therefore, the PI gains for the current control are:

$$K_i = L\omega_0^2 = 1.73 \times 10^4 \quad (52)$$

$$K_p = 2\xi\omega_0 L - R_s = 10.5 \quad (53)$$

Assuming the system is stable and once the system reaches steady state, there will be no change in time and therefore it can be shown mathematically that there is no steady state error, an important feature of an aerospace EMA:

$$\begin{aligned} \cancel{i''(t)} + \frac{R_s + K_p}{L} \cancel{i'(t)} + \frac{K_i}{L} i(t) &= \frac{K_p}{L} \cancel{i_{\text{ref}}'(t)} + \frac{K_i}{L} i_{\text{ref}}(t) \\ \frac{K_i}{L} i(t) &= \frac{K_i}{L} i_{\text{ref}}(t) \\ i(t) &= i_{\text{ref}}(t) \end{aligned}$$

6 Conclusions

This project successfully achieved the design and simulation of a control system for an EMA suitable for a MEA aileron application. The selected actuator, GS40-0602, along with its corresponding PMM, met all specified performance requirements. The control system was built using a cascade architecture with nested current, speed, and position loops, enabling clear timescale separation and good dynamic response.

Each control loop was designed based on second-order system theory, with parameters selected based on damping ratio and bandwidth separation. The current loop featured cross-coupling compensation and an anti-windup mechanism, the latter proving highly effective under saturation scenarios. SIMULINK[®] simulations validated that the system responded rapidly and accurately to step inputs and disturbances without overshoot in the position domain — a critical requirement for aerospace actuators.

Notable challenges included managing the transient distortion caused by zeros in the system's transfer function, which was mitigated through input lag filtering in the position loop. The simulation results demonstrated strong agreement with theoretical expectations, and the final system delivered strong tracking across all control domains.

Overall, the project demonstrated a comprehensive understanding of EMA architecture, modelling, and control design. The methodology presented here is transferable to a broad class of electric drive applications,

References

- [1] J. G. Leishman, *Introduction to Aerospace Flight Vehicles*. Embry-Riddle Aeronautical University, Jan. 2023, ISBN: 979-8-9852614-0-0. DOI: [10.15394/EAGLEPUB.2022.1066](https://doi.org/10.15394/EAGLEPUB.2022.1066).
- [2] P. Wheeler and S. Bozhko, 'The more electric aircraft: Technology and challenges,' *IEEE Electrification Magazine*, vol. 2, no. 4, pp. 6–12, Dec. 2014, ISSN: 23255889. DOI: [10.1109/MELE.2014.2360720](https://doi.org/10.1109/MELE.2014.2360720).
- [3] P. W. Wheeler, J. C. Clare, A. Trentin, and S. Bozhko, 'An overview of the more electrical aircraft,' *Proceedings of the Institution of Mechanical Engineers, Part G: Journal of Aerospace Engineering*, vol. 227, no. 4, pp. 578–585, Apr. 2013, ISSN: 09544100. DOI: [10.1177/0954410012468538](https://doi.org/10.1177/0954410012468538).
- [4] G. Qiao, G. Liu, Z. Shi, Y. Wang, S. Ma, and T. C. Lim, 'A review of electromechanical actuators for More/All Electric aircraft systems,' *Proceedings of the Institution of Mechanical Engineers, Part C: Journal of Mechanical Engineering Science*, vol. 232, no. 22, pp. 4128–4151, Nov. 2018, ISSN: 20412983. DOI: [10.1177/0954406217749869/ASSET/8CA56283-5D12-4DB2-8375-7522620C9E2A/ASSETS/IMAGES/LARGE/10.1177{_}0954406217749869-FIG14.JPG](https://doi.org/10.1177/0954406217749869/ASSET/8CA56283-5D12-4DB2-8375-7522620C9E2A/ASSETS/IMAGES/LARGE/10.1177{_}0954406217749869-FIG14.JPG).
- [5] P. Wheeler, 'Technology for the more and all electric aircraft of the future,' *2016 IEEE International Conference on Automatica, ICA-ACCA 2016*, Dec. 2016. DOI: [10.1109/ICA-ACCA.2016.7778519](https://doi.org/10.1109/ICA-ACCA.2016.7778519).
- [6] A. Garcia, J. Cusidó, J. A. Rosero, J. A. Ortega, and L. Romeral, 'Reliable electro-mechanical actuators in aircraft,' *IEEE Aerospace and Electronic Systems Magazine*, vol. 23, no. 8, pp. 19–25, Aug. 2008, ISSN: 08858985. DOI: [10.1109/MAES.2008.4607895](https://doi.org/10.1109/MAES.2008.4607895).
- [7] J. R. Leigh, 'Control theory,' p. 297, 2004.